Compressible impurity flow in the TJ-II stellarator

J Arévalo[1], J A Alonso[1], K J McCarthy[1], J L Velasco[1], J M García-Regaña[2] and M Landreman[3]

[1] Laboratorio Nacional de Fusión, Asociación EURATOM-CIEMAT, Madrid, Spain
[2] Max-Planck-Institut für Plasmaphysik, EURATOM-Assoziation, Garching, Germany
[3] Plasma Science and Fusion Center, MIT, Cambridge, Massachusetts, USA

E-mail: juan.arevalo@externos.ciemat.es

Abstract. Fully-ionised carbon impurity flow is studied in ion-root, neutral beam heated plasmas by means of Charge Exchange Recombination Spectroscopy (CXRS) in the TJ-II stellarator. Perpendicular flows are found to be in reasonable agreement with neoclassical calculations of the radial electric field. The parallel flow of the impurity is obtained at two locations of the same flux surface after subtraction of the calculated Pfirsch-Schlüter parallel velocity. For the medium density plasmas studied, $\bar{n}_e \in (1.2-2.4) \times 10^{19}$ m^{-3}, the measured impurity flow is found to be inconsistent with a total incompressible flow, i.e. $\nabla \cdot \mathbf{u}_z \neq 0$, thus implying a non-constant impurity density on those flux surfaces. The experimentally observed velocity deviations are compared with the parallel return flow calculated from a modelled impurity density redistribution driven by ion-impurity friction. Although the calculated return flow substantially modifies the incompressible velocity pattern, the modifications at the precise locations of the CXRS measurements are generally smaller in magnitude and opposite in sign as compared to the experimentally observed deviations. Small inhomogeneities of the electrostatic potential in a surface are also shown to affect the impurity redistribution but do not provide a better understanding of the measurements.

1. Introduction

The flow of mass along flux surfaces in magnetically confined plasmas has come to be regarded as an important factor in determining plasma stability, radial transport and performance of these devices. The $E \times B$ flow pattern is of particular importance with regard to transport. Indeed, a sufficiently strong radial velocity shear is generally accepted as reducing turbulence and transport [1]. The flow patterns of the different species present in the plasma (main ions, electrons and impurity ions) deviate from the $E \times B$ flow and from each other through their different diamagnetic velocity components and parallel force balances. These diamagnetic and parallel flows give rise to currents that are a fundamental part of the stellarator MHD equilibrium in high-beta reactor-relevant plasmas. Parallel currents are generally split into Pfirsch-Schlüter (PS) and parallel mass flows. The former arises in response to the compressibility of the perpendicular diamagnetic current and carries no net toroidal current, but can nevertheless cause a radial (Shafranov) shift of magnetic surfaces as

the pressure gradient increases. The reduction of this current is a design requirement of modern stellarators because of its detrimental effect on high beta stability and neoclassical transport [2]. On the other hand, the bootstrap current carries a net toroidal current‡ and can potentially change the iota profile, which is of particular importance for island divertor configurations in stellarators and is taken advantage of in tokamak non-inductive scenarios. For these reasons experimental validation of first-principle theory-based models of plasma flows and currents is of considerable importance. In reference [4] measurements of fully ionised carbon impurity flow were undertaken using Charge Exchange Recombination Spectroscopy [5] (CXRS) in low density, Electron Cyclotron Resonance heated plasmas in the TJ-II stellarator. It was verified that the in-surface variation of the parallel impurity flow was consistent with an incompressible total flow tangent to flux surfaces. In addition, the measured perpendicular and parallel mass flows were compared with neoclassical calculations of the radial electric field and ion parallel mass flow, finding a good agreement in those low density plasmas.

In this work, CXRS measurements of C^{6+} flows in Neutral Beam Injection (NBI) heated, ion-root plasmas of the TJ-II stellarator are presented. As indicated in reference [4] significant and reproducible deviations in the measured impurity flow from an incompressible pattern are observed as density increases, which points to a redistribution of impurity density within the flux surfaces. We present these flow measurements and compare the observed deviations with the parallel return flow from a modelled impurity density redistribution driven by ion-impurity friction [6]. Such a friction model was adapted to a general stellarator geometry with the bulk ions in the Pfirsch-Schlüter regime of collisionality in reference [7] and is extended here for main ions in the plateau regime, provided the ion temperature gradient is small (a plausible assumption for the plasmas under consideration). The calculated return flow substantially modifies the incompressible velocity pattern, being comparable to the impurity parallel PS flow. However, it is shown that the calculated modifications at the precise locations of the CXRS measurements are small in comparison to the measured in-surface variations of impurity parallel flow and in the opposite direction for most cases. The inclusion of inertial and parallel electric field forces in the parallel momentum balance does not provide a better understanding of the experimental observations.

The fact that impurity density inhomogeneities can alter the radial transport of impurities [6] makes the understanding of these inhomogeneities particularly relevant. Also, from the data interpretation point of view, the parallel return flows associated to the density inhomogeneity might complicate the comparison of CXRS rotation measurements to standard neoclassical theory, particularly in the presence of large main-ion gradients [8, 9]. Observations of in-out flow variations have been reported in the CHS stellarator [10] and the C-Mod and ASDEX-U tokamaks [11, 12], which have been recently shown to be caused by a poloidal redistribution of the impurities with direct impurity density measurements [13, 14]. In this work we restrict ourselves to the discussion of flow deviations from incompressibility as an indirect measure of the C^{6+} density inhomogeneity, since several instrumental uncertainties of the TJ-II CXRS system prevent the interpretation of signal intensities as relative density measurements. On the other hand, parallel and perpendicular impurity flows and

‡ In the parallel mass flow we therefore include all the relevant parallel forces that determine the parallel flows of the different species, e.g. the NBI-driven currents. It is also noted that, to some extent, the split of the parallel currents is a matter of convention [3].

temperatures are routinely provided by the CXRS system and have been shown to be in fair agreement with other diagnostics and/or neoclassical theory predictions [4, 15].

This paper is organised as follows: in section 2, the diagnostic set-up and geometry are presented together with the methodology used to relate the flow fields to the CXRS velocity measurements through the appropriate geometric quantities. In section 3 the impurity flow measurements and their compressible asymmetries are described. These asymmetries are compared with the results of an ion-impurity friction model in section 4, where modifications to the incompressible impurity flow pattern, caused by an in-surface impurity density variation, are detailed. In section 5 the validity of the friction model is examined and the impurity parallel force balance is extended to account for inhomogeneities of the electrostatic potential within a magnetic surface. Finally, conclusions are drawn in section 6.

2. Diagnostic set-up and data analysis

The CXRS process of interest in TJ-II involves electron capture from accelerated hydrogen by fully ionized carbon ions into a highly excited state of C^{5+}, followed by spontaneous decay via photon emission, i.e. the C VI line at 529.07 nm ($n = 8 \rightarrow 7$). For this, a compact Diagnostic Neutral Beam Injector (DNBI) provides a 5 ms long pulse of neutral hydrogen accelerated to 30 keV. Its $1/e$-radius at focus is 21 mm [16].

Correctly performed instrument wavelength calibration and optical alignment are essential to minimize the CXRS experimental uncertainties. For the first case, a neon pencil lamp is inserted between each light collection lens and corresponding fibre head between discharges to determine the wavelength dispersion at the focal plane for each fibre. In addition, corrections are made for fine-structure, Zeeman broadening and the so-called pseudo-velocities [17] before Doppler shifts and widths are determined. The uncertainties associated with the integration of geometrical quantities along sight lines are also accounted for. See reference [4] for a complete description. In this way, the uncertainty achieved in measured velocity is 1 to 2 km s^{-1} (except at the innermost toroidal line sight where it increases by times 2 or 3 due to poor photon statistics).

The procedure for aligning the diagnostic is detailed in section 2.1 of reference [4]. The location of the flux surfaces is known accurately from the vacuum field. Note that the helical axis of TJ-II makes the Shafranov shift very small (3 mm) even for 1 beta values (see e.g., A. Varias et al. NF 30, (1990), 2597. "Ideal Mercier Stability for the TJ-II Flexible Heliac").. This shift is much less than the spot size of the fibers.. Consequently, the inboard and outboard measurements are directly mapped to flux coordinates using the known magnetic field geometry, and in contrast to the tokamak experiments [11, 12, 14], no additional relative shift between the inboard and outboard measurements is needed to align the carbon temperature profiles. Moreover, an additional check to confirm the goodness of the toroidal ρ mapping is made. For this, the spectrograph grating (set at 529 nm [16]) was exchanged for one centred at 656.2 nm. Then, by injecting the DNBI beam into the vacuum chamber with no magnetic fields, spectra with Doppler-shifted H$_\alpha$ line emission from the beam were collected and analysed. Hence, by determining the Doppler shift of the beam H$_\alpha$ for each sight line, the corresponding beam velocity was calculated without correcting for the beam to sight line angle. Knowing the beam energy, the beam to sight line angles were determined and the beam/sight line intersection points could be determined. These intersection points were compared with the values obtained using the illumination method described in [4] thereby confirming the uncertainties in the

alignment of toroidal fibres, i.e. $\sim \pm 3$ mm. Note: the separation between toroidal sightlines, ≥ 3 cm, is fixed by the fibre bundle and focusing lens.
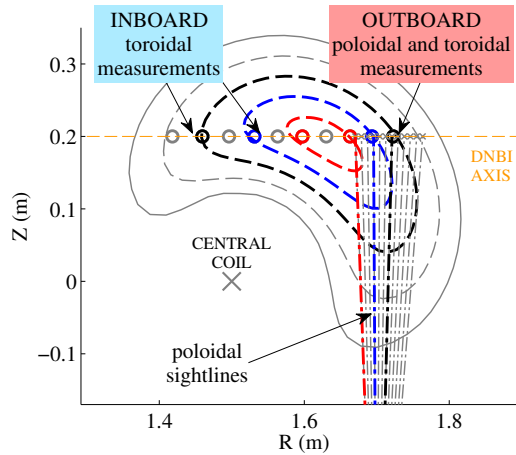
Figure 1. Schematic diagram of CXRS diagnostic sightlines with a poloidal cut of several magnetic surfaces of TJ-II. The inboard and outboard regions of measurement are highlighted. The magnetic surfaces in which poloidal and toroidal outboard measurements are coincident, $\rho \sim 0.2, 0.4$ and 0.6, are coloured in red, blue and black, respectively.

A schematic layout of the diagnostic sightlines is presented in figure 1, together with a poloidal cut of several magnetic surfaces of TJ-II. The plasma minor radius region spanned by nearly symmetric poloidal views is $\rho \in (0.25, 0.85)$ in the magnetic configurations studied in this work. Here the normalised radius is defined as $\rho \equiv \sqrt{V/V_0}$, where V and V_0 are the volumes enclosed by the surface of interest and the last closed magnetic surface, respectively. In the figure only the bottom poloidal array is presented for clarity (see reference [4] for details). On the other hand, the toroidal fibres cover both sides of the magnetic axis, from $\rho \sim -0.75$ to $\rho = 0.6$ at 10 locations (in figure 1 the toroidal sightlines, plotted as open circles, go outside the page). The region in which both poloidal and toroidal measurements are taken is labelled as outboard, while the zone where only toroidal measurements are made is labelled as inboard. The nomenclature $\rho \geq 0$ (outboard) and $\rho \leq 0$ (inboard) is also utilized to define these regions.

In the outboard region, poloidal and toroidal fibres view the same surfaces at $\rho \sim 0.2, 0.4$ and 0.6, see figure 1. Therefore, the 2D-flow velocity is completely determined at these locations. The redundant inboard-toroidal measurements have been recently used to demonstrate that, in low density TJ-II plasmas (with line-averaged electron densities $\bar{n}_e \leq 10^{-19}$ m^{-3}), impurity rotation is incompressible and follows neoclassical theory [4]. The general form of the impurity flows and the methodology used to asses their incompressibility is described next.

2.1. Spatial variation of the flow

From the radial force balance for a single species s it follows that the perpendicular velocity is given by the $\mathbf{E} \times \mathbf{B}$ and diamagnetic flows [19],

$$\mathbf{u}_{s\perp} = \frac{\mathbf{B}}{B^2} \times \left(\nabla\Phi + \frac{1}{n_s q_s} \nabla p_s \right) + \mathcal{O}(\delta_s^2 v_s). \tag{1}$$

where n_s, $q_s = eZ$ and $v_s = \sqrt{2T_s/m_s}$ are the density, charge and thermal velocity of the species s, and $\delta_s = \rho_s/L$ is the gyro-radius over system scale ratio. In the following the subscript i is used for main-ions and z for impurities with charge Z. The impurity diamagnetic term in equation (1) is usually neglected against the $E \times B$ flow, that is generally comparable to the main ion diamagnetic term. We will adopt this approximation for the C^{6+} ions used in our measurements. The perpendicular impurity ion flow is then given by

$$\mathbf{u}_{z\perp} = E_z \frac{\mathbf{B} \times \nabla\rho}{B^2}, \quad E_z = \frac{\mathrm{d}\Phi}{\mathrm{d}\rho} \tag{2}$$

where Φ is the electric potential. We have neglected any parallel variation of Φ against the radial variation in this expression. From main ions, the perpendicular diamagnetic flow is included in $E_i(\rho) = \mathrm{d}\Phi/\mathrm{d}\rho + (n_i e)^{-1}\mathrm{d}p_i/\mathrm{d}\rho$

Given the form of the perpendicular s flow, the parallel component is obtained from the (steady-state) s number conservation, $\nabla \cdot (n_s \mathbf{u}_s) = 0$. If density of s is constant on flux surfaces then $\nabla \cdot \mathbf{u_s} = 0$ and a local parallel flow (Pfirsch-Schlüter) must compensate for the compression of the perpendicular flows. The general expression of the parallel flow is then (see e.g. [4, 20])

$$\mathbf{u}_{s\parallel} = (E_s(\rho)h + \Lambda_s(\rho))\,\mathbf{B}, \tag{3}$$

with the function $h(\rho, \theta, \phi)$ (θ, ϕ: poloidal and toroidal angles) satisfying

$$\mathbf{B} \cdot \nabla h = \frac{2}{B^2}\mathbf{B} \times \nabla\rho \cdot \nabla(\ln B).$$

The integration constant for h is fixed by the condition $\langle hB^2 \rangle = 0$. With this choice the flux-constant $\Lambda_s(\rho)$ in (3) is given by $\Lambda_s = \langle \mathbf{u}_s \cdot \mathbf{B} \rangle / \langle B^2 \rangle$, where $\langle \cdot \rangle$ denotes a flux-surface average. The first term on the right of equation (3), $\mathbf{u}_{\mathrm{PS}} = E_s h\mathbf{B}$, is the well-known Pfirsch-Schlüter. Hereafter, $\Lambda_s\mathbf{B}$ is referred as the parallel mass flow of the s species, i.e. the parallel flow without the PS contribution.

In our previous work [4] we showed that the above expressions for an incompressible impurity flow pattern agreed well with the C^{6+} CXRS measurements in low density plasmas. The so-obtained $E_z(\psi)$ and $\Lambda_z(\psi)$ were found to be agreement with neoclassical calculations of the ambipolar radial electric field and main ion parallel mass flow, $\langle \mathbf{u}_i \cdot \mathbf{B} \rangle / \langle B^2 \rangle$, respectively. For the higher density plasmas under study in this work we observe a systematic deviation of the parallel flows from the form given by equation (3). The deviation is interpreted to be caused by variations of impurity density n_z within the flux surfaces, in which case the reduction of the number conservation condition to the incompressibility of total impurity flows no longer holds. We treat this situation by allowing the function Λ_z to have angular dependencies. To quantify the deviations it is convenient to define an impurity parallel return flow as $\Lambda(\rho, \theta, \phi) = \Lambda_z(\rho, \theta, \phi) - \Lambda_i(\rho)$, which is associated with parallel gradients of the impurity density. With this particular choice, impurity flows are written as the sum of an incompressible flow,

$$\mathbf{u}_{z0} = E_z \frac{\mathbf{B} \times \nabla\rho}{B^2} + (\Lambda_i + E_z h)\,\mathbf{B}, \tag{4}$$

plus the return flow, $\Lambda\mathbf{B}$, which compensates for the impurity density redistribution, i.e.

$$\mathbf{u}_z = \mathbf{u}_{z0} + \Lambda(\rho,\theta,\phi)\mathbf{B}. \tag{5}$$

Note that this velocity field is the same as that given by equations (2) and (3), but with $\Lambda_z(\rho,\theta,\phi) = \Lambda(\rho,\theta,\phi) + \Lambda_i(\rho)$. The case $\Lambda = 0$ reduces to an incompressible flow pattern with the z impurities dragged by the ion parallel flow, i.e. $\Lambda_z = \Lambda_i(\rho)$.

2.2. Data analysis

The data analysis here presented is an adaptation of that of ref. [4] to account for the possible compressible variations of the parallel impurity flow just discussed. The method makes use of the three independent flow measurements performed at the same flux surface (two of them also at the same point in the surface, refer to figure 1) to obtain independent measurements of the parallel impurity flow Λ_z at two locations of the same flux surface. The logic can be summarised as follows: first the intersecting poloidal and toroidal outboard sight lines are used to extract the local parallel and perpendicular flows. The perpendicular flow provides a direct estimate of $E_z(\rho)$, which is then used to subtract the Pfirsch-Schlütercomponent from the parallel velocity to get a first measurement of $\Lambda_z^{\mathrm{Out}} = \Lambda_z(\rho,\theta^{\mathrm{Out}},\phi^{\mathrm{Out}})$. The obtained value of $E_z(\rho)$ can also be used to calculate the projections of the perpendicular and parallel Pfirsch-Schlüterflows on the inboard toroidal measurement at the same flux surface. After subtraction of these projections we obtain a second value, $\Lambda_z^{\mathrm{In}} = \Lambda_z(\rho,\theta^{\mathrm{In}},\phi^{\mathrm{In}})$, of the parallel mass flow of the impurity ion.

To make the above description more explicit we define the dimensionless vector $\mathbf{f}$ as

$$\mathbf{f} = -\frac{\langle B\rangle}{\langle|\nabla\rho|\rangle}\left(\frac{\mathbf{B}\times\nabla\rho}{B^2} + h\mathbf{B}\right) \tag{6}$$

and the average radial electric field and perpendicular velocity as $E_{\mathrm{r}}(\rho) \equiv -\langle|\nabla\rho|\rangle\mathrm{d}\Phi/\mathrm{d}\rho$ and $U_\perp(\rho) \equiv E_{\mathrm{r}}/\langle B\rangle$ respectively. The impurity flow given by equation (5) is expressed as

$$\mathbf{u}_z = \mathbf{f}U_\perp + \Lambda_z\mathbf{B}. \tag{7}$$

Once the value of $U_\perp(\rho)$ is calculated from the intersecting poloidal and toroidal sight lines at the outboard region, the quantity $\Lambda_z(\rho,\theta,\phi)$ is obtained after projecting this flow onto the toroidal sight lines,

$$\Lambda_z = \frac{u_{\mathrm{t}} - f_{\mathrm{t}}U_\perp}{B_{\mathrm{t}}}. \tag{8}$$

Here, the sub-index t indicates the projection of a vector ($\mathbf{u}$, $\mathbf{f}$ and $\mathbf{B}$) in the toroidal viewing direction, $\mathbf{e}_{\mathrm{t}}$. Finally, the differences in the parallel mass flow (divided by the local magnetic field strength) are

$$\Delta\Lambda_z = \Delta\left(\frac{u_{\mathrm{t}}}{B_{\mathrm{t}}}\right) - U_\perp\Delta\left(\frac{f_{\mathrm{t}}}{B_{\mathrm{t}}}\right), \tag{9}$$

where $\Delta(X) \equiv X^{\mathrm{In}} - X^{\mathrm{Out}}$. Note that the differences in the impurity parallel mass flow equal those of the impurity return flow defined in equation (5), i.e. $\Delta\Lambda_z = \Delta\Lambda$. Therefore, if flows are incompressible, Λ_z is a flux function proportional to the $U_b(\rho)$ defined in [4]. The in-out differences in Λ_z (see figure 3 of section 3) can then be

compared with the symmetry in U_b profiles found in low density density plasmas (figures 7 and 10 of that reference).

The perpendicular flow constant $U_\perp$ is obtained at three radial positions ($\rho \sim 0.2, 0.4$ and 0.6, see figure 1). We use these values together with the condition $U_\perp(0) = 0$ to interpolate $U_\perp$ at the radial locations of all CXRS toroidal measurement and obtain a Λ_z profile from equation (8). Figure 3 shows several examples of these profiles, that are discussed in the next section.

3. Experimental results

In this work, two close magnetic configurations are considered: 100_44_64 and 100_40_63. Here, the nomenclature reflects currents in the central, helical and vertical coils, respectively. On-axis magnetic field is about 1 T. The vacuum rotational transform, t, covers the range $1.55 \leq t \leq 1.65$ and $1.509 \leq t \leq 1.608$, and the volumes are 1.098 and 1.043 m^3, respectively. These two configurations have been studied in references [21] and [22] from the neoclassical point of view. For similar plasma profiles and momentum input, no qualitative differences are predicted in the flows within the surface. The plasmas presented here are heated by one of the two tangential NBI ($t_{NBI} \leq 100$ ms), either in the direction of the magnetic field (co-injection), or in the opposite direction (counter-injection). The line averaged densities scanned in this paper cover the range $\bar{n}_e \in (1.2 - 2.4) \times 10^{19}$ m^{-3}.
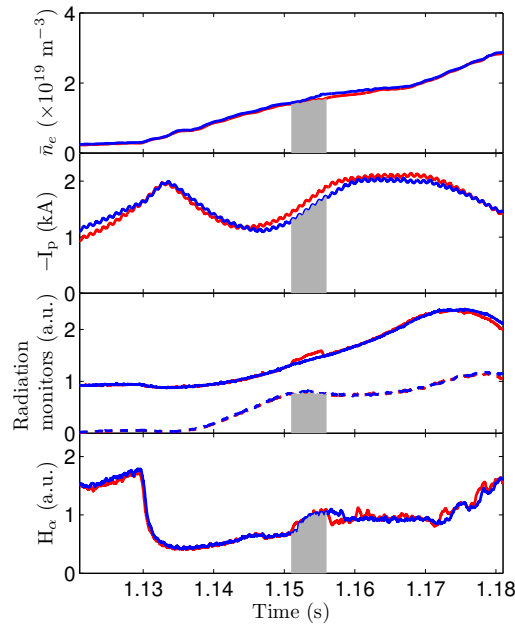
Figure 2. Time evolution of two similar plasma discharges. In red, shot#32577 with a DNBI pulse and in blue, shot#32576 without DNBI, used to remove the C^{5+} passive contribution. From top to bottom, time traces of: line averaged electron density, $\bar{n}_e$; plasma current (reversed), $-I_p$; radiation monitors: bolometer (solid line) and C^{4+} (dashed); H_α signal. The DNBI injection is shown in grey.

Time traces of a representative plasma discharge, #32577, in the 100_44_64 configuration are shown in figure 2. The evolution of the reference discharge (#32576) used to remove background C^{5+} emission is in blue, whilst the one in which the DNBI was fired, #32577, is in red. The time interval in which the DNBI is injected is plotted as a grey shadow. The NBI heating causes an increase in the line-averaged density and radiation. The radiation monitors in figure 2 correspond to a bolometer signal (whose view-line intersects the DNBI path) and a C^{4+} monitor, shown as solid and dashed lines, respectively. A small increase is observed in the bolometer signal for discharge #32577, which corresponds to photon excitation induced by the DNBI. Finally, the plasma current, I_p, is negative corresponding to counter-injection (a co-injection reverses the sign of the current). The small oscillation observed in the plasma current is produced by small variations in the current of the external coils. The good reproducibility of the two discharges shown in figure 2 is representative of the data set used in this work and allows an accurate subtraction of the background C^{5+} emission from the active DNBI discharge.
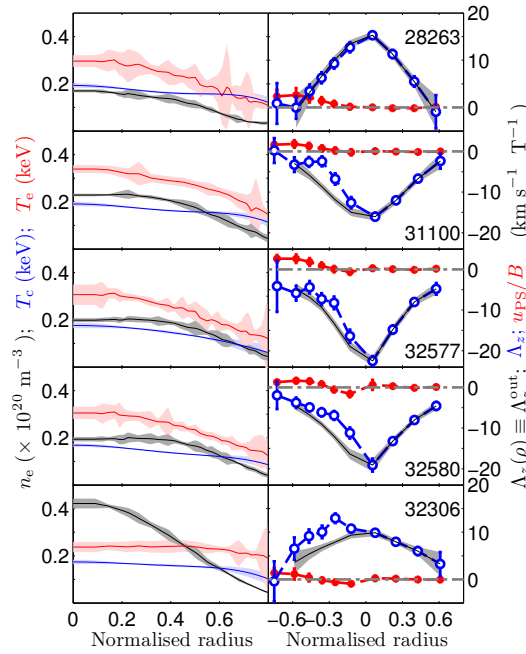
Figure 3. Left: profiles of the electron density (n_e, in gray) and temperature (T_e, in red), together with carbon temperature profiles (T_c, in blue). Right: measured profile of Λ_z, in blue, and the incompressible expectation extrapolated from the outboard measurements, in grey. The calculated Pfirsch-Schlüter contribution is displayed in red. The discharge #28263, in which flows were demonstrated to be incompressible [4], is included here as a reference. The discharges #31100, #32577 and #32580, heated with one NBI in counter-injection (consistent with $\Lambda_z < 0$) are presented to highlight the reproducibility of the departure from incompressibility observed in Λ_z. Discharges #31100 and #32306 were performed in the configuration 100_40_63.

Electron density and temperature profiles (n_e and T_e, respectively) are measured by the Thomson scattering diagnostic [18], see figure 3. The discharges in the figure

were performed in the 100-44-64 magnetic configuration, except discharges #31100 and #32306 (configuration 100-40-63). In all the discharges considered in this paper, the electron temperature profile is approximately parabolic, with $T_{\mathrm{e}}(0) \approx 300$ eV, whilst the carbon temperature profile is rather flat, with $100 \leq T_{\mathrm{c}} \leq 200$ eV (it is assumed that main ion and impurities are in thermal equilibrium). In the right column of figure 3 the C^{6+} parallel mass flow, $\Lambda_z \mathbf{B}$, and PS flow, $\mathbf{u}_{\mathrm{PS}} = E_z h \mathbf{B}$, contributions to the total parallel velocity, $\mathbf{u}_\parallel = \mathbf{u}_{\mathrm{PS}} + \Lambda_z \mathbf{B}$, are shown in blue and red, respectively (see section 2 for an explanation of the extraction of these flow components from the experimental measurements). The direction of the bulk toroidal flow is mainly determined by the NBI momentum injection. The incompressible expectation extrapolated from the outboard measurements, i.e. $\Lambda_z = \Lambda_z(\rho) = \Lambda_z^{\mathrm{Out}}$, is shown in grey. The discharge #28263 is heated by the co-NBI injector and shows a lower line-averaged density ($\bar{n}_{\mathrm{e}} = 1.2 \times 10^{19}$ m^{-3}). For this low-density NBI discharge flows were shown to be incompressible in reference [4], and is included here as a reference. The measured Λ_z profile departs from the incompressible expectation in the co-NBI discharge #32306 and the counter-NBI discharges #31100, #32577 and #32580. The reproducibility of the Λ_z profile for these similar discharges in terms of $n_{\mathrm{e}}, T_{\mathrm{e}}$ and T_{c} profiles, but otherwise distant in time and impurity content, reinforces the reproducibility of the observed flow deviations. The general tendency observed in the experimental database, with few exceptions, is that the inboard parallel flow is more positive than the outboard one, and thus, the in-out differences in the parallel mass flow, $\Delta \Lambda_z$ from equation (9), are always positive. This observation is nearly independent on the magnetic configuration and the direction of injection of the heating NBIs.
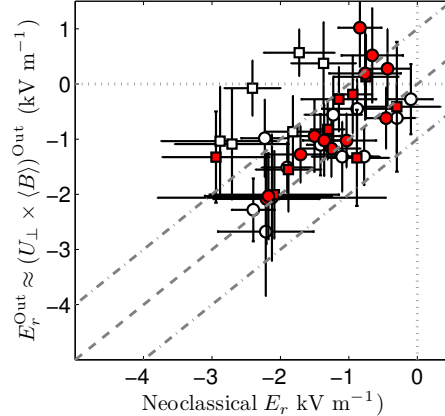
Figure 4. Comparison of the experimentally measured radial electric fields for the outboard region, E_r^{Out}, with the corresponding neoclassical values for several TJ-II discharges. Dashed lines correspond to the NC value (diagonal) and the region of confidence $E_r^{\mathrm{Out}} = E_r^{\mathrm{NC}} \pm 1$ kV m^{-1} (upper and lower diagonals). Here, circles and squares represent data from the 100-44-64 and 100-40-63 magnetic configurations, respectively. Red points indicate NBI in counter-**B** direction (consistent with $\Lambda_z < 0$) while white points indicate co-injection. Note that the impurity diamagnetic term is not included in computing the measured E_r (see text).

As indicated in section 2, toroidal and poloidal view lines of the CXRS system

overlap at three locations ($\rho \approx 0.2, 0.4$ and 0.6) on the outboard side of the DNBI path. This enables unambiguous determination of the perpendicular and parallel flow components at those locations, relying only on the assumption of a small radial flow component compared to perpendicular and parallel flows. The perpendicular impurity flow component is expected to be dominated by the $E \times B$ flow because of the $1/Z$ factor of the diamagnetic flow. Figure 4 shows the comparison of this experimental approximation to the radial electric field with the neoclassical expectations, calculated as in [22]. The database shown here is comprised of 12 discharges. Data taken in the 100_44_64 and 100_40_63 magnetic configurations are presented as circles and squares, respectively. Note that the impurity diamagnetic term is not included in the calculation of the experimental radial electric field, because of the uncertainties in determining the carbon density profile in TJ-II. Nevertheless, a rough estimate of the diamagnetic contribution (obtained from the CXRS signals while ignoring the calibration deficiencies mentioned in section 2) typically results in absolute values ≤ 1 kV m^{-1} at $\rho = 0.6$, with little or no impact for more internal regions, as expected from the $1/Z$ dependence. This estimation is consistent with the main-ion diamagnetic velocities calculated form experimental data, $|v_{\mathrm{diam},i}| \leq 4$ km s^{-1} for $|\rho| \leq 0.6$.

Despite this uncertainty in the estimated radial electric field, we note that the radial electric field does not enter any of the expressions for the impurity flows alone (sections 2.1 and 4), but rather in combination with the diamagnetic component as the total perpendicular flow. Such a velocity component is provided by the overlapping CXRS velocity measurements through geometric factors only and is not subjected to such uncertainties. In the following, the measured parallel mass flow deviations in the region $|\rho| \in (0.2, 0.6)$ are studied on the light of an impurity density redistribution model.

4. Friction-driven impurity density redistribution

Impurity temperature and parallel mass flow are generally taken to be a proxy of those of the main ions, as the impurity fluid is typically strongly collisionally coupled to the main ion fluid. For similar temperatures ($T_z \approx T_i$) and large mass difference ($m_z \gg m_i$), impurity z and ion i collisionalities relate to each other through $\hat{\nu}_{zi} = (m_i/m_z)^{1/2}(q_z/q_i)^2\hat{\nu}_{ii}$ with $\hat{\nu}_{ab} = \nu_{ab}R/(tv_a)$ (see e.g. [23]). The pre-factor is ~ 10 for Hydrogen plasma and C^{6+} impurity which, for the plateau ions characteristic of TJ-II [22], places the impurity under study in the Pfirsch-Schlüter collisional regime. This collisional character of medium to high-Z impurities can cause their density variations within a surface to be comparable with the mean value on that surface [6], and thus, the impurity parallel mass flow to differ from that of the main-ions. In order to study the measured parallel mass flow deviations from an incompressible pattern, the continuity equation

$$\mathbf{B} \cdot \nabla \left(\frac{n_z u_{z\parallel}}{B} \right) = -E_z \mathbf{B} \times \nabla\rho \cdot \nabla \left(\frac{n_z}{B^2} \right), \tag{10}$$

and the impurity parallel force balance

$$T_z \nabla_\parallel n_z = R_{z\parallel}, \tag{11}$$

need to be solved for the unknown functions n_z and Λ_z. Here, $R_{z\parallel}$ is the parallel friction on the impurities. The inclusion of other forces in (11) (namely the impurity inertia and the parallel electric field) is described and evaluated in section 5, while the impurity parallel viscosity is neglected against the parallel impurity pressure gradient,

$\nabla_{\parallel} p_z$ [6]. As also shown in reference [6], the strong ion-impurity energy equilibration keeps the impurity temperature close to the ion one and thus $T_z = T_i(\rho)$.

In terms of the Λ function defined in (5) and $n \equiv n_z/\langle n_z \rangle$ these two equations are written as

$$\mathbf{B} \cdot \nabla(n\Lambda) = -\mathbf{u}_{z0} \cdot \nabla n, \qquad (12a)$$

$$\mathbf{B} \cdot \nabla \ln n = \gamma_{\mathrm{f}} B^2 \left(A_{\mathrm{i}} h + B_{\mathrm{i}} - \Lambda \right), \qquad (12b)$$

whose solubility condition is $\langle \Lambda B^2 \rangle = B_i(\rho)\langle B^2 \rangle$, see the Appendix A. The compressible pattern (5) has been used to express the continuity equation (10) in its form (12a). In addition, a flux-constant friction coefficient $\gamma_{\mathrm{f}}(\rho)$ and thermodynamic forces $A_{\mathrm{i}}(\rho)$ and $B_{\mathrm{i}}(\rho)$ have been defined in (12b) as

$$\gamma_{\mathrm{f}} \equiv \frac{m_i Z^2}{T_{\mathrm{i}} \tau_{ii}}, \qquad (13a)$$

$$A_{\mathrm{i}} \equiv \frac{T_{\mathrm{i}}}{e} \frac{\mathrm{d} \ln n_{\mathrm{i}}}{\mathrm{d}\rho} - \frac{1}{2e} \frac{\mathrm{d} T_{\mathrm{i}}}{\mathrm{d}\rho}, \qquad (13b)$$

$$B_{\mathrm{i}} \equiv -\frac{3}{5} \frac{\langle \mathbf{q}_{\mathrm{i}} \cdot \mathbf{B} \rangle}{p_{\mathrm{i}} \langle B^2 \rangle}, \qquad (13c)$$

with $\tau_{ii} = 3(2\pi)^{3/2} \varepsilon_0^2 m_i^{1/2} T_i^{3/2}/(n_i e^4 \ln \Lambda)$ the ion self-collision time and $\mathbf{q}_i$ the ion heat flow. In deriving expression (12b) trace impurities are considered, $\sum n_z Z^2 \ll n_i$, and so the parallel friction on the impurities is approximated by that exerted by main ions, i.e. $R_{z\parallel} \approx R_{zi\parallel} = -R_{iz\parallel}$. The ion-impurity collision operator is modelled with a Lorentz pitch-angle scattering operator plus a term guaranteeing momentum conservation [6]. Finally, no assumption is made on bulk ion's collisionality since its distribution function is expanded by Legendre and Laguerre polynomials, as is customary in the so-called moment approach to neoclassical transport [20, 23]. Here, the so-called 13 M approximation [24] is adopted, i.e. contributions from $j > 1$ Laguerre components are neglected, see the Appendix A. We note that in the axisymmetric tokamak case, the impurity continuity equation (10) yields an algebraic relationship between the parallel impurity flow and the impurity density (see e.g. [25]), whereas such a simplification does not occur in general stellarator geometry [7].

The ion-impurity parallel friction is studied first in the next subsection. The effect of a parallel electric field and impurity inertial forces are considered in section 5. We anticipate here that the parallel momentum balance is dominated by the friction force and that the general behaviour of the solutions is to display $\Delta \Lambda_z < 0$, in contrast with the measured in-out variation. This can be heuristically understood by noting that the differences in the Pfirsch-Schlüter flow, $A_i h B$ in equation (12b), drive the impurity density redistribution. As a consequence of the in-surface density variation, an impurity return flow ΛB is established (equation (12a)) which must act to reduce the overall ion-impurity friction so that the density redistribution is not further amplified. Since the term $A_i h$ on the RHS of equation (12b) is more negative at the inboard side, the return flow Λ tends to behave similarly.

4.1. Calculation of the friction-driven impurity redistribution

The two coupled equations (12a) and (12b) can be recast as a second order partial differential equation for the unknown function $n(\rho, \theta, \phi)$ (see Appendix A). The radial

coordinate is a parameter in those equations which involve angular derivatives only. The required inputs are the main ion parameters (temperature T_i, density n_i, parallel mass flow Λ_i and flux-surface averaged parallel heat flow $\langle \mathbf{q}_i \cdot \mathbf{B} \rangle$) together with the impurity perpendicular flow. The CXRS and Thomson scattering systems provide measurements of these parameters, except for the ion parallel mass and heat flows. The latter is calculated with DKES [26], complemented with momentum correction techniques [27]. On the other hand, the measured Λ_z in the outboard region is used as a first guess for the ion parallel mass flow to solve the differential equations, $\Lambda_i^{(0)} = \Lambda_z^{\text{Out}}$, since the external input of momentum is not included in the DKES Λ_i calculations [21]. A new guess for the main ion parallel flow is then obtained upon subtraction of the calculated impurity-ion flow difference, $\Lambda^{(0)}$ in our notation, i.e. $\Lambda_i^{(1)} = \Lambda_z^{\text{Out}} - \Lambda^{(0)}$. Note that at every step momentum conservation is imposed, i.e. $\langle \Lambda B^2 \rangle = B_i(\rho)\langle B^2 \rangle$ from equation (12b). The iteration of this process leads to a solution for the impurity flow that matches the outboard CXRS measurement, $\Lambda_z^{(n+1)} \equiv \Lambda_i^{(n+1)} + \Lambda^{(n)} = \Lambda_z^{\text{Out}}$. In practice only one iteration is necessary because the impurity return flow Λ is not very sensitive to the ion parallel flow Λ_i and the outboard measurement locations happen to be close to a stagnation point of the calculated impurity return flow, so that $\Lambda_i = \Lambda_z^{\text{Out}}$ is already a good guess.
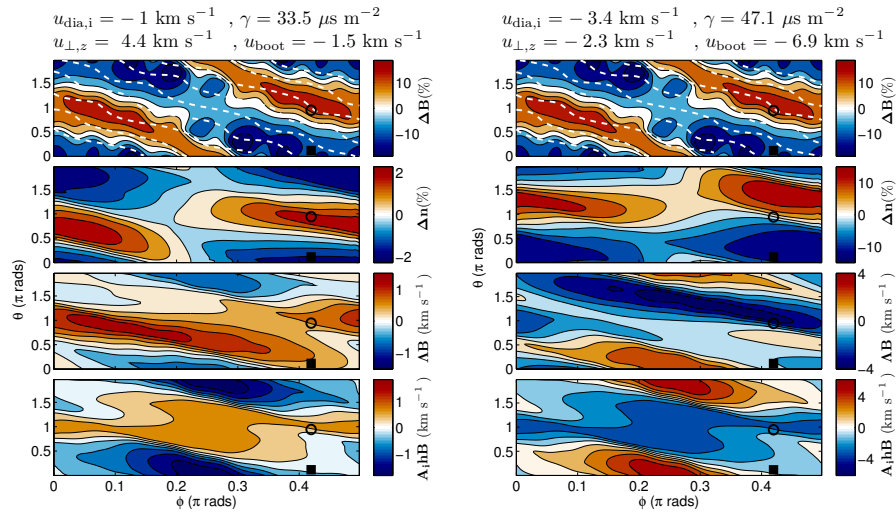
Figure 5. C^{6+} impurity density redistribution simulation for the discharges #25801 (left) and #32577 (right) on the surface $\rho = 0.6$. From top to bottom: magnetic field strength variation, $\Delta B = B/\langle B \rangle - 1$ (field lines are plotted in white); density variation, $\Delta n = n_z/\langle n_z \rangle - 1$; return parallel flow, ΛB; and the differences in the Pfirsch-Schlüter velocity, $\Delta u_\parallel^{PS} \sim A_i hB$. The inboard/outboard toroidal measurement positions are shown as an open circle and filled square, respectively.

An example of the solution is shown in figure 5 for discharge #32577 presented in figures 2 and 3 and for the $\rho = 0.6$ magnetic surface. These results correspond to fully ionised carbon C^{6+} impurity that is used for the CXRS measurements. From top to bottom the relative variations of magnetic field strength B and impurity density, the corresponding impurity return flow and the parallel friction drive $A_i hB$

are plotted. The inboard/outboard toroidal measurement positions are shown as an open circle and solid square, respectively. As a reference the same quantities obtained for the low-density ECRH heated discharge #25801 are presented. The slightly hollow density profiles in typical ECRH discharges in TJ-II results in a small and negative thermodynamic force A_i, see equation (13a). Correspondingly, both the relative impurity density variations and return flow are small. Plasma profiles and CXRS flow measurements for this discharge can be found in reference [4]. In particular we recall that the measured impurity flows were shown to be nearly incompressible for this discharge.
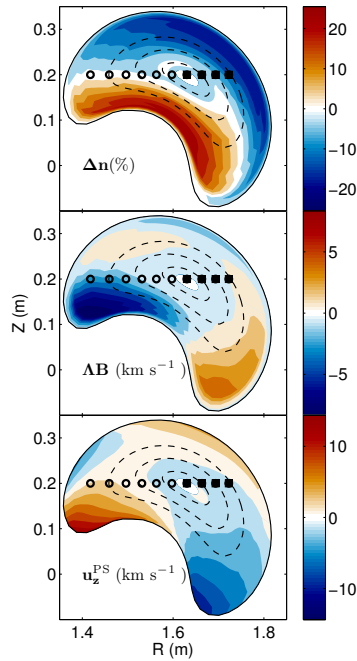
Figure 6. Mapping of C^{6+} impurity density redistribution simulation in the CXRS poloidal plane of measurement for the discharge #32577. From top to bottom: density variation, $\Delta n = n_z/\langle n_z \rangle - 1$; impurity return flow, ΛB; and the impurity Pfirsch-Schlüter velocity. The inboard and outboard toroidal measurement positions are shown as open circles and filled squares, respectively.

The results of the calculations of impurity density redistribution for discharge #32577 and for several magnetic surfaces, $\rho \leq 0.8$, are plotted in figure 6 for the toroidal section of the CXRS measurements, $\phi = 75.5^{\circ}$. Again, the inboard and outboard toroidal measurement positions are shown as open circles and filled squares, respectively. The magnetic surfaces in which the inboard/outboard comparison is made, namely $\rho \sim 0.2, 0.4$ and 0.6, are also shown as dashed lines. The first two graphs of the figure are the normalized impurity density redistribution, $\Delta n = n_z/\langle n_z \rangle - 1$, and impurity return flow, ΛB. The Pfirsch-Schlüter impurity flow, $u_z^{PS} = E_z hB$, is presented at the bottom of the figure.

Some general comments on the solution can be made in light of the simulation results shown in figures 5 and 6. For the plasma profiles of the database used in this work, $\bar{n}_e \in (1.2-2.4) \times 10^{19}$ m^{-3}, carbon impurities tend to accumulate in the interior

region of the bean-shaped plasma poloidal cross section (which is close the region of maximum magnetic field strength in TJ-II due to the proximity of the central coil). The resulting return flow is comparable in size to the PS impurity flow. Its angular dependence also shows a dominant $\cos\theta$ component. The difference in sign between the PS and return parallel flows is in line with the overall tendency heuristically described at the beginning of this section: the return flow Λ tends to compensate the $A_i hB$ friction drive in equation (12b), for in these ion-root plasmas A_i and $\mathrm{d}\Phi/\mathrm{d}\rho$ are of similar magnitude and different signs so that $u_z^{PS} \approx (\mathrm{d}\Phi/\mathrm{d}\rho)hB \sim -A_i hB$. Consequently, the differences in the calculated impurity parallel return flow at the locations of the CXRS measurements, $\Delta\Lambda_z \equiv \Delta\Lambda$ from (5), are found to be negative for the ion-root plasma discharges in our CXRS database.

4.2. Comparison with experiment
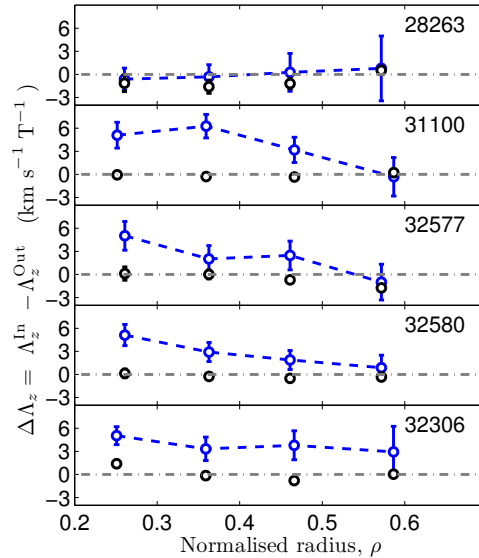
Figure 7. Radial profiles of the friction-driven simulated (black) and experimental (blue) differences in the parallel mass flow $\Delta\Lambda_z$, for the same discharges presented in figure 3.

Figure 7 shows the radial profiles of the friction-driven simulated (black) and experimental (blue) differences in the impurity parallel mass flow, $\Delta\Lambda_z$, for the discharges presented in figure 3. The calculated compressible modifications to the impurity flow become small at the locations of CXRS measurements and do not account for the observed differences. A comparison of the experimental and theoretical values of $\Delta\Lambda_z$ is presented in figure 8 for the same database as in figure 4. Error bars in figures 7 and 8 come from the spread of the calculated velocities in the measurement volumes. As discussed in section 4.1, the parallel friction term in equation (12b) calculated from experimental profiles appears capable of producing a measurable impurity density asymmetry and parallel return flow, even for the internal positions considered in this work (the region of maximum gradient is typically

located at $\rho \sim 0.7 - 0.8$ in TJ-II plasmas). Values of $\Delta\Lambda_z^{\text{theo}} \sim -2$ km s^{-1} T^{-1}, or larger, are found in the simulation, while the experimental differences can easily reach $\Delta\Lambda_z^{\text{exp}} \sim 6$ km s^{-1} T^{-1}. The overall tendency of the calculated return flows to be more negative in the inboard side is also clear from figure 8. Note that at the inboard positions the impurity return flow varies sharply, see figure 5, which translates into large error bars.
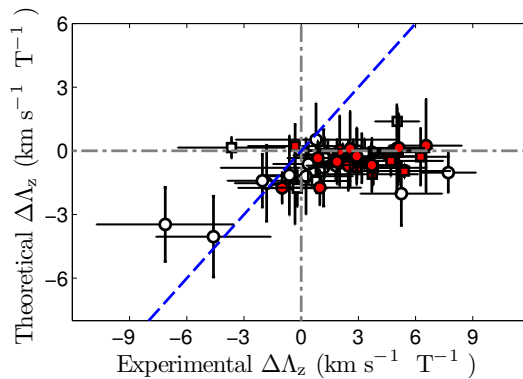
Figure 8. Comparison of the experimental and theoretical values of $\Delta\Lambda_z$. It is observed that the expected and measured values are systematically in disagreement, except for a few values. The symbols legend is the same as in figure 4. The error bars in the simulation come from the spread of the calculated velocities in the measurement volumes.

From this comparison it is concluded that, whereas the impurity-ion parallel friction (in its model form in equation (12b)) is capable of causing impurity density asymmetries and return flows of the order of magnitude of the observed in-out flow differences, the calculated return flows do not agree with the observed in-surface variation of the impurity parallel mass flow Λ_z at the locations of the CXRS measurements for most cases. In the following section some of the assumptions made in the model (12b) are examined, and the parallel force balance (11) is extended to account for the impurity inertia and the effect of a parallel electric field.

5. Discussion on the validity and extensions of the model

Previous impurity parallel friction models for stellarators [7] consider main ions in the Pfirsch-Schlüter regime. This regime is not strictly applicable to the plasmas presented here ($n_{\text{i}} \in (0.5 - 3) \times 10^{19}$ m^{-3}, $T_{\text{i}} \in 100 - 200$ eV) since main ions are in the plateau regime $\hat{\nu}_{ii} \sim 10^{-1} - 10^{0}$ [22]. As indicated in section 4 and explained in the Appendix A, no assumption is made in this work on bulk ion collisionality, although the main ion distribution function is truncated in the Laguerre expansion ($j \leq 1$, see Appendix A) as in the 13 M approximation [23, 24].

In order to quantify the impact of this approximation let us consider main ions in the Pfirsch-Schlüter regime, as in reference [7]. In this regime of collisionality $\langle \mathbf{q}_i \cdot \mathbf{B} \rangle = 0$ (hence $B_i = 0$ in (13c)) and $A_i^{\text{PS}} = (T_i/e) \times (\mathrm{d}\ln n_i/\mathrm{d}\rho)$. Now, if the $j > 1$ truncation is applied to the exact collisional result, the thermodynamic force A_i
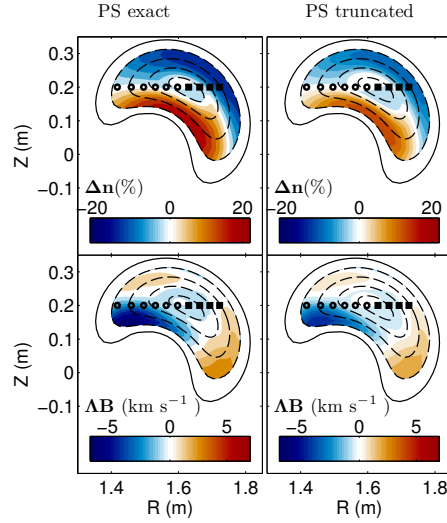
Figure 9. Mapping of C^{6+} impurity density redistribution and return flow in the CXRS polodial plane of measurement for the discharge #32577. On the left, the exact Pfirsch-Schlüter main ion distribution function is used [7].On the right, the $j > 1$ truncation is applied to the PS exact result.

in (12b) results

$$A_i^{\text{PS, truncated}} = A_i^{\text{PS}} - \frac{1}{2e}\frac{dT_i}{d\rho},$$

which equals the general result A_i in (13c). The resultant impurity redistribution and return flow as obtained from the exact and truncated collisional results are displayed in the left and right columns of figure 9, respectively. As observed, the impurity density in-surface variation reaches values up to $\Delta n \sim \pm 20$ % in the exact collisional result while $\Delta n \sim \pm 13$ % is found when truncating the main ion distribution function. The simulated return velocity, ΛB, is similarly affected by the truncation (values of ± 6 and ± 4 km s^{-1} are obtained in the exact and truncated friction models, respectively). The comparison in figure 9, and the proximity of TJ-II main ion collisionalities to the Pfirsch-Schlüter regime, indicate that the inclusion of higher order Legendre components [24] in the modelled friction (12b) is unlikely to change the tendencies in the simulated impurity redistribution and return flow presented in section 4. On the other hand, the generalization of the parallel friction presented in (12b) allows us to directly use the measured main-ion parameters (since no assumption is made on collisionality) and to include the effect of a non-zero parallel heat flow, thus extending previous friction models in stellarators [7].

Besides the above discussion on the generalization of the ion-impurity parallel friction, the impurity parallel force balance (11) can be extended to account for inertial and electrostatic parallel forces as

$$m_z n_z \mathbf{b} \cdot (\mathbf{u}_z \cdot \nabla \mathbf{u}_z) + n_z Z e \nabla_\parallel \Phi + T_z \nabla_\parallel n_z = R_{z\parallel}, \tag{14}$$

where the first term is the impurity parallel inertia and the second one is the parallel electric field. The former can be approximated by

$$m_z n_z \mathbf{b} \cdot (\mathbf{u}_z \cdot \nabla \mathbf{u}_z) \approx m_z n_z \Lambda_i^2 \mathbf{B} \cdot \nabla B,$$

since the local PS and return parallel flows are expected to be smaller than the main ion parallel mass flow in internal regions $|\rho| \leq 0.4$ of TJ-II NBI heated plasmas. This same approximation leads to the centrifugal outboard accumulation of high-Z impurities in tokamaks [28]. In order to examine the impact of the inertia on the impurity density redistribution, let the impurity parallel force balance be dominated by the inertia, i.e. $\nabla_\parallel \ln n_z = -\gamma_c^2 \nabla_\parallel b^2$ with $b \equiv B/\langle B \rangle$, $\gamma_c(\rho) \equiv \Lambda_i \langle B \rangle / v_z$ and $v_z = \sqrt{2T_z/m_z}$ the impurity thermal velocity. Then the impurity inhomogeneity is $\Delta n = \exp\left(-\gamma_c^2 [b^2 - 1]\right)$. Note that although main ion parallel mass flows ≤ 20 km s^{-1} are comparable to thermal velocities ≤ 50 km s^{-1} (i.e. $\gamma_c \leq 0.4$), the large aspect ratio of TJ-II $(b^2 - 1) \sim a/R \sim 0.1$ makes $\Delta n \leq 2$ % for all the plasma minor radius (here, $a \sim 0.2$ m and $R = 1.5$ m are the minor and major plasma radius). Such an estimation has been confirmed numerically. Therefore, the impurity inertia is neglected henceforth.

On the other hand, the term containing the electrostatic potential variation in the flux surface, $\tilde{\Phi} = \Phi - \langle \Phi \rangle$, in equation (14) is considered. This portion of the full electrostatic potential, Φ, results from imposing quasi-neutrality among the non-equilibrium density pieces of the coexistent species. Furthermore the calculation, carried out with the particle in cell code EUTERPE [29], considers adiabatic electron response and trace impurities. Under these approximations the resulting map of $\tilde{\Phi}$ mirrors that of the main ion density. As an example, $\tilde{\Phi}$ is shown in figure 10 for the discharge #32577. On the left column, $\tilde{\Phi}$ at the surface $\rho = 0.6$ is represented, while on the right $\tilde{\Phi}$ is displayed at several magnetic surfaces, $\rho \leq 0.8$, for the toroidal section of the CXRS measurements.
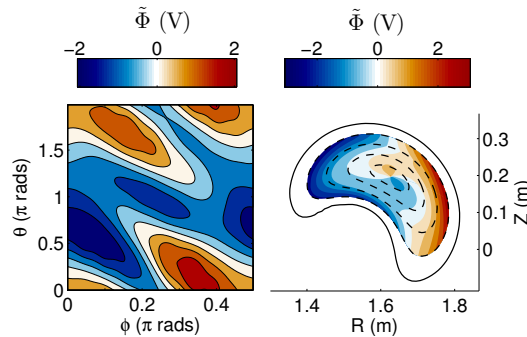
Figure 10. Simulation of the electrostatic potential inhomogeneity, $\tilde{\Phi}$ in Volts, for discharge #32577. (Left) In-surface variations for $\rho = 0.6$. (Right) Mapping in the CXRS poloidal plane for several magnetic surfaces, $\rho \leq 0.8$.

Thus, if parallel inertia is neglected, the impurity momentum balance (14) results as

$$\mathbf{B} \cdot \nabla \ln n = \gamma_f B^2 \left(A_i h + B_i - \Lambda \right) - \frac{eZ}{T_z} \mathbf{B} \cdot \nabla \Phi, \qquad (15)$$

The parallel momentum balance in its form (15), together with particle conservation (12a), can be transformed into a second order partial differential equation for the unknown n, as in section (4.1). Figure 11 displays a mapping in the CXRS poloidal plane of measurement of the simulation results for discharge #32577 and for several magnetic surfaces, $\rho \leq 0.8$, after considering (left) only friction and (right) friction

plus the $\nabla_\parallel \Phi$ forces in its model form (15). As observed, the impurity redistribution and return flow patterns are affected by the inhomogeneity of the potential only at external radial locations $\rho > 0.7$. Nevertheless the tendency to display $\Delta\Lambda < 0$ remains unaltered, thus contradicting the experimental observations.
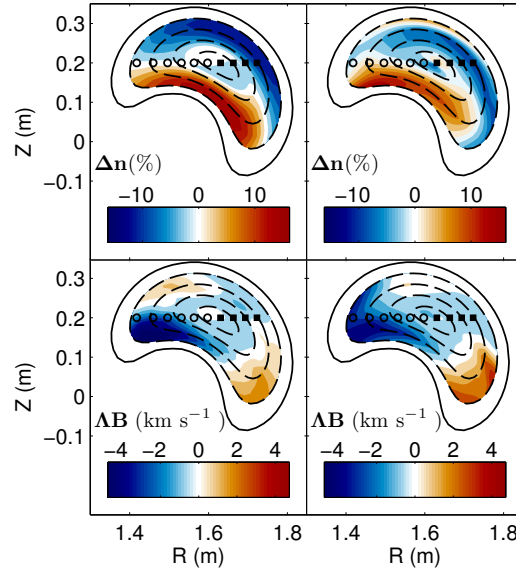
Figure 11. Mapping in the CXRS poloidal plane of the simulated C^{6+} density inhomogeneity, Δn, and return flow, $\Lambda\mathbf{B}$, for discharge #32577 and for several magnetic surfaces, $\rho \leq 0.8$, after considering: (left) friction only and (right) all the relevant forces in model (15).

Finally, a possibly important omission of the impurity re-distribution model used in this work could be the assumption of trace impurities. For the plasmas considered here values of $Z_{\text{eff}} \sim 1.2 - 1.6$ are obtained from soft X-ray emission, which would give rise to impurity strengths of $n_z Z^2 / n_i \sim 0.2 - 0.6$. In such a case both the inhomogeneity of the electrostatic potential [25] and the collision operator used to model the parallel friction on the impurities [14] would change, thus modifying the impurity redistribution within a magnetic surface. The inclusion of these effects is out of the scope of this paper and is left to future work.

6. Conclusions

In this work fully-ionised carbon impurity flows in ion-root, NBI heated, TJ-II plasmas are studied by means of Charge Exchange Recombination Spectroscopy. Perpendicular flows are found to be in reasonable agreement with neoclassical calculations of the radial electric field. The parallel flow of the impurity is obtained at two locations on the same flux surface and the calculated Pfirsch-Schlüter parallel velocity is subtracted. The remaining component of the flow is systematically observed to vary on each flux surface, pointing to a breakdown of impurity flow incompressibility in the medium density plasmas studied. The experimentally observed velocity deviations are compared with the parallel return flow calculated from a modelled impurity

density redistribution driven by ion-impurity friction. Such a model is extended to account for impurity inertia and inhomogeneities in the electrostatic potential. The simulation results show that the parallel impurity force balance is dominated by parallel friction for the plasmas considered here, and demonstrate that the calculated return flow substantially modifies the incompressible velocity pattern. However, these modifications become small at the locations of the CXRS measurements and do not explain the in-surface variations of impurity parallel flow. The experimental validation of theoretical models of impurity density redistribution within a flux surface is of considerable importance as it provides an indirect validation of the model predictions for impurity radial transport.

Acknowledgement

Appendix A. Impurity density redistribution in a stellarator

In this appendix the parallel momentum balance (15) is derived and the method used to solved this equation consistently with particle number conservation is detailed. The impurity parallel momentum equation is taken to be

$$T_z \nabla_\| n_z + n_z Z e \nabla_\| \Phi = R_{z\|}, \tag{A.1}$$

where $R_{z\|}$ is the parallel friction on the impurities and Φ the electrostatic potential. As demonstrated in reference [6] the impurity temperature is equilibrated with the bulk ion temperature and is therefore constant on the flux surface. As it is also shown in [6], impurity parallel inertia and viscosity can be neglected in (A.1) if $\delta_i/(Z\hat{\nu}_{ii}) \ll 1$. For the plasmas considered in this work ($n_i \in (0.5-3) \times 10^{19}$ m^{-3}, $T_i \in 100-200$ eV) typical values of the normalised ion gyro-radius are $\delta_i \sim (5-10) \times 10^{-3}$. Bulk ions in NBI-heated TJ-II plasmas are in the plateau regime, $\hat{\nu}_{ii} \sim 10^{-1}-10^0$, although close to the Pfirsch-Schlüter regime of collisionality [22]. Then, for fully-ionised carbon impurity ions ($Z = 6$), $\delta_i/(Z\hat{\nu}_{ii}) \sim 10^{-3}-10^{-2}$. Hence, the assumptions made in reference [6] to derive equation (A.1) are applicable in this work. Furthermore, the expected variations of C^{6+} density within the surface are $\tilde{n}_z/\langle n_z \rangle \sim \delta_i \hat{\nu}_{ii} Z^2 \sim 0.1-0.5$, thus justifying the present study.

In the trace impurity limit, $\sum n_z Z^2 \ll n_i$, the parallel friction on the impurities may be approximated by [25]

$$R_{z\|} \approx R_{zi\|} = -R_{iz\|} = -\int \mathrm{d}^3 v m_i v_\| C_{iz}\{f_{i1}\}, \tag{A.2}$$

with f_{i1} the first order departure of the bulk ion distribution function from a Maxwellian. The ion-impurity collision operator consists of a Lorentz operator plus a

term guaranteeing momentum conservation [23]

$$C_{iz}\{f_{i1}\} = \nu_{iz}\mathcal{L}\{f_{i1}\} + \nu_{iz}\frac{m_i v_\| u_{z\|}}{T_i}f_{i0}, \tag{A.3}$$

$$\mathcal{L} = \frac{1}{2}\frac{\partial}{\partial\xi}\left[(1-\xi^2)\frac{\partial}{\partial\xi}\right]. \tag{A.4}$$

Here, $\nu_{iz} = 3\pi^{1/2}/(4\tau_{iz}x_i^3)$, $\tau_{iz} = \tau_{ii}n_i/(n_z Z^2)$ is the ion-impurity collision time, $x_i = v/v_i$, $v_i = \sqrt{2T_i/m_i}$ the ion thermal speed, $\xi = v_\|/v$ the pitch-angle and $f_{i0} = n_{i0}/(\pi^{3/2}v_i^3)\exp\left(-x_i^2\right)$ is a flux-function Maxwellian. Since the collision operator is self-adjoint and $\mathcal{L}\{v_\|\} = -v_\|$, the term in the parallel friction force arising from the Lorentz operator is written as

$$-\int d^3 v\, m_i v_\| \nu_{iz}\mathcal{L}\{f_{i1}\} = \frac{3\pi^{1/2}}{4\tau_{iz}}m_i v_i \int d^3 v \frac{\xi}{x_i^2}f_{i1}. \tag{A.5}$$

Let us consider now the expansion of $f_{i1}(\mathbf{x},v,\xi)$ in Legendre polynomials $P_l(\xi)$ [$P_0 = 1$, $P_1 = \xi$, etc.] [20]. Thanks to the orthogonality properties of the P_l polynomials only the $l = 1$ component of f_{i1} contributes to equation (A.5). Such component is associated with the parallel particle and heat flows ($u_{i\|}$ and $q_{i\|}$, respectively) and is expanded by Laguerre (Sonine) polynomials $L_j^{(3/2)}(x_i^2)$ $\left[L_0^{(3/2)} = 1,\ L_1^{(3/2)} = -x_i^2 + 5/2,\ L_1^{(3/2)} = x_i^4/2 - 7x_i^2/2 + 15/8,\text{ etc.}\right]$ as [20, 23]

$$f_{i1}^{(l=1)} = \frac{2}{v_i}\xi x_i\left\{u_{i\|} - L_1^{(3/2)}(x_i^2)\frac{2}{5}\frac{q_{i\|}}{p_i}\right\}f_{i0} + f_{i1}^{(l=1,j\geq 2)}. \tag{A.6}$$

Here, $f_{i1}^{(l=1,j\geq 2)}$ denotes the sum of the jth Laguerre polynomial components with $j \geq 2$. The inclusion of $j > 1$ terms [24] is out the scope of this paper and thus $f_{i1}^{(l=1)} \approx f_{i1}^{(l=1,j\leq 1)}$ is taken in equation (A.6), as it is customary in the moments approach to neoclassical transport [23] (the so-called 13 M approximation). See the comments in section 5 regarding the effect of this truncation. With this assumption the parallel friction on the impurities reads

$$R_{z\|} \approx \frac{m_i n_{i0}}{\tau_{iz}}\left(u_{i\|} - \frac{3}{5}\frac{q_{i\|}}{p_i} - u_{z\|}\right), \tag{A.7}$$

with $u_{z\|}$ the impurity ion parallel flow. § For simplicity energy exchange is neglected, thus making heat flows incompressible for each particle species, $\nabla\cdot\mathbf{q}_\alpha \approx 0$. Then the bulk ion parallel heat flow is

$$q_{i\|} = \frac{5p_i}{2e}\frac{\partial T_i}{\partial\rho}hB + \langle\mathbf{q}_{i\|}\cdot\mathbf{B}\rangle\frac{B}{\langle B^2\rangle}, \tag{A.8}$$

with the function h defined in section 2.1. Using the general expression for a compressible impurity flow, equation (5), and equation (A.8), the parallel friction on the impurities is finally recast as

$$\begin{aligned}R_{z\|} &= \frac{m_i n_{i0}}{\tau_{iz}}B\left(\left[E_i - E_z - \frac{3p_i}{2e}\frac{\partial T_i}{\partial\rho}\right]h - \Lambda - \frac{3}{5}\frac{\langle\mathbf{q}_{i\|}\cdot\mathbf{B}\rangle}{p_i\langle B^2\rangle}\right) \\ &\approx p_z\gamma_f B\left(A_i h + B_i - \Lambda\right),\end{aligned} \tag{A.9}$$

§ Note that if the exact result for main ion distribution function in the Pfirsch-Schlüter regime is used [7]

$$f_{i1}^{(l=1)} = \frac{2}{v_i}\xi x_i\left\{u_{i\|} - \left(L_1^{(3/2)}(x_i^2) - \frac{4}{15}L_2^{(3/2)}(x_i^2)\right)\frac{2}{5}\frac{q_{i\|}}{p_i}\right\}f_{i0},$$

the pre-factor $-3/5$ accompanying the parallel heat flow in (A.7) must be replaced by $-2/5$.

with the flux constants $\gamma_f(\rho)$, $A_i(\rho)$ and $B_i(\rho)$ given by equations (13). In the last step, the impurity diamagnetic term has been neglected against the main ion one. With these assumptions (i.e. trace impurities, $\sum n_z Z^2 \ll n_i$, and 13 M approximation, $f_{i1}^{(l=1)} \approx f_{i1}^{(l=1,j\leq1)}$) the impurity parallel momentum balance (A.1) results

$$\mathbf{B} \cdot \nabla n_z = \gamma_{\mathrm{f}} n_z B^2 \left(A_i h + B_i - \Lambda\right) - n_z \frac{eZ}{T_z} \mathbf{B} \cdot \nabla \Phi, \tag{A.10}$$

hence recovering equation (14) and the simplified form (12b), when the inhomogeneity of the potential, $\tilde{\Phi} \equiv \Phi - \langle\Phi\rangle$, is neglected. In stellarator geometry, equation (A.10) and the continuity equation (10) form a coupled system [7] of partial differential equations (PDEs). This set of equations can be expressed as a parabolic PDE in the variable $n = n_z/\langle n_z \rangle$

$$\mathbf{B} \cdot \nabla \left(\mathbf{B} \cdot \nabla n\right) - g\mathbf{B} \cdot \nabla n - \gamma_{\mathrm{f}} B^2 \mathbf{u}_{z\perp} \cdot \nabla n - fn = 0, \tag{A.11}$$

where

$$g(\rho,\theta,\phi) = \mathbf{B} \cdot \nabla \ln B^2 - \frac{eZ}{T_z} \mathbf{B} \cdot \nabla \Phi +$$
$$\gamma_{\mathbf{f}} B^2 \left\{(A_i + E_z)h + B_i + \Lambda_i\right\}, \tag{A.12}$$
$$f(\rho,\theta,\phi) = \gamma_{\mathrm{f}} A_i \mathbf{B} \times \nabla \rho \cdot \nabla \ln B^2 +$$
$$\frac{eZ}{T_z} \left(\mathbf{B} \cdot \nabla \ln B^2 - \mathbf{B} \cdot \nabla\right) \mathbf{B} \cdot \nabla \Phi. \tag{A.13}$$

Equation (A.11) is converted to an algebraic system of equations by applying finite differences to the variable n. The angular periodicity of the TJ-II ($T_\theta = 2\pi$ and $T_\phi = \pi/2$) and the condition $\langle n \rangle = 1$ are imposed. The parallel return flow ΛB is obtained from equation (12a). The system of PDEs has also been solved by Fourier expanding the variables in Boozer coordinates, showing consistency with the finite differences scheme.

References

[1] Terry P.W. 2000 *Rev. Mod. Phys.* **72** 109
[2] Wobig H. 1999 *Plasma Phys. Control. Fusion* **41**, A159
[3] Coronado M. and Wobig H. 1992 *Phys. Fluids B* **4**, 1294
[4] Arévalo J. *et al* 2013 *Nucl. Fusion* **53** 023003
[5] Isler R. C. 1994 *Plasma Phys. Control. Fusion* **36** 171
[6] Helander P. 1998 *Phys. Plasmas* **5** 3999
[7] Braun S. and Helander P. 2010 *J. Phys.: Conf. Series* **260** 012004
[8] Solomon W.M. *et al* 2006 *Phys. Plasmas* **13** 056116
[9] Tala T. *et al* 2007 *Nucl. Fusion* **47** 1012
[10] Nishimura S. *et al* 2000 *Phys. Plasmas* **7** 437
[11] Marr K. D. *et al* 2010 *Plasma Phys. Control. Fusion* **52** 055010
[12] Pütterich T. *et al* 2012 *Nucl. Fusion* **52** 083013
[13] Churchill R. M. *et al* Poloidal Flows and In-Out Impurity Density Asymmetries in the Pedestal Region, 2012 *APS Conf. Plasma Phys. (Providence, USA).* Available on-line at `https://www.psfc.mit.edu/research/alcator/pubs/APS/APS2012/Churchill_APS2012_cont-oral.pdf`
[14] Viezzer E. *et al* Rotation and density asymmetries in the presence of large poloidal impurity flows in the edge pedestal, 2013 *EPS Conf. Plasma Phys. (Espoo, Finland).* Available on-line at `http://ocs.ciemat.es/EPS2013ABS/pdf/I4.112.pdf`
[15] Velasco J. L. *et al* Vanishing neoclassical viscosity and physics of the shear layer in stellarators, 2013 *EPS Conf. Plasma Phys. (Espoo, Finland).* Available on-line at `http://www-fusion.ciemat.es/Jose_Luis_Velasco/presentations/velasco_etal_EPS2013.pdf`
[16] Carmona J M *et al* 2006 *Rev. Sci. Instr.* **77** 10F107
[17] Bell R.E. and Synakowski E.J. 2000 *AIP Conf. Proc.* **547** 39

[18] van Milligen B. Ph. 2011 *Rev. Sci. Instrum.* **82** 073503
[19] Hinton F. L. and Hazeltine R. D. 1976 *Rev. Mod. Phys.* **48** 239
[20] Sugama H. and Nishimura S. 2002 *Phys. Plasmas* **9** 4637
[21] Velasco J. L. *et al* 2011 *Plasma Phys. Control. Fusion* **53** 115014
[22] Velasco J. L. and Castejón F. 2012 *Plasma Phys. Control. Fusion* **54** 015005
[23] Helander P. and Sigmar D.J. 2002 *Collisional Transport in Magnetized Plasmas*, Cambridge
       Univ. Press
[24] Nishimura S. *et al* 2011 *Phys. Plasmas* **18** 069901
[25] Landreman M., Fülöp T. and Guszejnov D. 2011 *Phys. Plasmas* **18** 092507
[26] Hirshman S.P. *et al* 1986 *Phys. Fluids* **29** 2951
[27] Maassberg H. *et al* 2009 *Phys. Plasmas* **16** 072504
[28] Reinke M. L. *et al* 2012 *Plasma Phys. Control. Fusion* **54** 045004
[29] García-Regaña J. M. *et al* 2013 *Plasma Phys. Control. Fusion* **55** 074008